The semidiurnal tide for individual nights derived consistently from O$_2$ and OH intensities and temperatures

Esteban R. Reisin* and Jürgen Scheer

Instituto de Astronomía y Física del Espacio, CONICET - Universidad de Buenos Aires. Buenos Aires, Argentina.

* Corresponding author: Esteban R. Reisin, Instituto de Astronomía y Física del Espacio, Ciudad Universitaria, C.C. 67 Suc. 28, 1428 Buenos Aires, Argentina (ereisin@iafe.uba.ar).

Abstract

The semidiurnal tide is studied with 159 special cases from the large airglow database acquired at El Leoncito (31.8ºS, 69.3ºW). These cases correspond to nights which exhibit similar periods in the temperature and intensity variations of the OH(6-2) and O$_2b$(0-1) emissions. We find that all the periods (except one) are between 9 and 15.5 hours. The phase distributions of these cases are narrow enough to ensure the identification as the semidiurnal tide, and their progression with altitude is consistent with downward phase propagation. The mean temperature amplitudes are large for both emissions. We obtain new values for Krassovsky's ratio including its phase. The vertical wavelength is determined independently for each emission using the relation suggested by the Hines and Tarasick theory. Mean vertical wavelengths derived for O$_2$ are longer than those for OH. The longest monthly mean wavelengths are observed from May to August. The mean ratio of temperature amplitudes between the two emissions corresponds to moderate wave attenuation during the upward propagation of the tide.

Keywords: Airglow; Mesopause region; Semidiurnal tide; Vertical wavelength

1. Introduction

Tides in the mesopause region have been observed with satellite and ground-based data (e.g., the temperature tides studied more recently by Mulligan and Nallen, 1998; Takahashi et al., 1998; López-González et al., 2005 and 2017; Pancheva et al., 2009; Azeem et al., 2016). Almost all of these studies are based on monthly means, or on running means over several days. Satellite data may give an extensive geographical coverage and, in this way, the different migrating and non-migrating tidal modes can eventually be distinguished (e.g. Pancheva et al., 2009; Azeem et al., 2016). However, satellite observations are not suitable to determine tidal characteristics with high temporal resolution.

On the other hand, ground-based measurements allow to monitor the tide during individual days (or nights). However, in order to be able to compare with models, the traditional approach is to extract tidal information from runs of many days. In this way, the effects of the day-to-day tidal variability, which the models are still unable to express, are removed. For example, the recent paper by Conte et al. (2018) on tidal observations with meteor radars used a sliding data window of 21 days and compared with the HAMMONIA model. In an opposite example, the semidiurnal tide was derived from wind data (through OH and OI airglow observations) for individual 24-hour intervals (Fisher et al., 2002). These authors confirmed that the semidiurnal tide is indeed "... *highly variable in amplitude and phase from day to day*".

At a single location, it is impossible to separate the different migrating and non-migrating tidal modes. However, such a separation is not necessary to study the net effect of tidal variability at the site. On the other hand, the spectral characterization of the tide from single-day data series is complicated by the effects of non-stationarity. These effects are due to the variations of background wind and temperature profile, which affect both the sources and the vertical propagation of the tide. Another complicating factor is the interference of other unrelated atmospheric waves which spectral analysis cannot always separate well. At any rate, the superposition of the different migrating and non-migrating tidal modes leads to *"a whole spectrum of tides propagating from the troposphere to the MLT"* (Forbes et al., 2006) instead of the fixed values suggested by tidal theory. However, all these problems cannot persist permanently, but must occasionaly be small enough to be negligible. At those times, useful information on tides can be obtained without major difficulty.

Using our extensive database of airglow measurements at El Leoncito, here we analyze the characteristics of the semidiurnal tide during single nights, for those special cases when the tide is documented self-consistently in the intensity and temperature of the OH and O_2 emissions. The nominal emission heights can be assumed to be 87 km for OH and 95 km for O_2 but the exact values do not matter in the present context. We make use of the possibility, opened by the theory of Hines and Tarasick (1987), to determine the vertical wave propagation (not only wavelength, but also whether the propagation is upward or downward) from each of the two airglow emissions. This self-consistent approach had already been used, although on a very limited scale, with our earliest data from Argentina and Spain (Reisin and Scheer, 1996, hereafter RS96).

2. Data and analysis method

The data used correspond to airglow zenith measurements of the O_2b(0-1) and OH(6-2) bands acquired between 1998 and 2014 with the Argentine Airglow Spectrometer (Scheer, 1987; Scheer and Reisin, 2001) located at "Complejo Astronómico El Leoncito" (CASLEO, at 31.8ºS, 69.3ºW). Band intensities and rotational temperatures for both emissions can be obtained simultaneously with a time resolution of about 80 seconds. To help ensure good-quality tidal results, we limit the analysis to nights with at least 250 data for each of the four parameters (i.e., 6 hours of good data, not counting gaps). With this ad hoc criterium, 2879 nights are still available from the 4034 nights with data. This data acquisition yield has been remarkably successful, for a non-commercial instrument operating remotely (see http://www.iafe.uba.ar/aeronomia/Months.html). Note that, in comparison to these 2879 nights, our earlier results (RS96) were based on only 85 nights (from five campaigns between 1986 and 1992).

For each of the four parameters comprising the nocturnal dataset, the frequency, amplitude, and phase of the principal spectral component are fitted as free parameters.

The spectral method consists in the determination of the frequency of the main spectral component of a least-squares-fit periodogram, similar to Lomb's scheme (Lomb, 1976), but with the constant term included (and therefore not necessarily equal to the mean).

The inclusion of the constant term in the fit is particularly important for periods longer than the data span, as is nearly always the case in our data. This spectral method was developed by Reisin (1994) (see

http://www.iafe.uba.ar/aeronomia/thesis/Reisin_thesis_apend.pdf where "Apéndice A" gives the mathematical derivation of the algorithm, with *a* and *b* from eq. A.6 defining the amplitude and phase in the usual way, and *K* from eq. A.4 is the constant term), and has been used frequently in the past (e.g., Scheer et al., 1994; Reisin and Scheer 1996; 2001; 2017).

As already mentioned, the tide in the mesopause region can vary considerably from day to day. It can even be present in one emission and absent in the other one (e.g., Scheer and Reisin, 1990). Because of the strong day-to-day tidal variability, it is reasonable to focus here on those nights that show consistent tidal signatures in the four parameters. For each of the two emissions, we select only the cases in which the frequencies of the intensity and temperature oscillation for the same airglow emission are sufficiently similar to improve the chance that both parameters are affected by the same wave. A maximum difference of 6 µHz has been found adequate; this corresponds to a difference of about 3.1 hours near a period of 12 hours.

We use only the subset of special cases when the oscillations in **both** emissions have closely similar frequencies, within the same 6 µHz tolerance as that used for the intensities and temperatures of a single emission. These are the cases which we call "self-consistent". To each of these cases, we assign a nominal frequency equal to the average for the four parameters. This still leaves us with a dataset of 159 nights. These cases, when the same wave manifests itself in both emissions, are particularly valuable for a number of geophysical reasons, including the comparison of vertical wavelengths at the two emission heights, amplitude growth factors, etc.

Each of the 12 months is well represented in the input of 2879 nights to our analysis, with from 155 to 309 nights per month (see Table 1). The monthly distribution of the 159 self-consistent cases studied here is strong and uniform from April to August. On the other hand, there are only a few cases in November and February, and none in December and January (see Table 1). Normalizing the number of the special cases by the monthly data coverage, we estimate the probability to find a special case in each month (column four in Table 1). Between April and August, this probability is highest, namely about 9%. According to our earlier findings (Reisin and Scheer, 2017), these are also the months of strong tidal activity. There we had shown, based on a monthly mean tidal climatology obtained independently for O_2 and OH, that the semidiurnal tide at El

Leoncito is strong between April and September, and nearly absent between November and February.

Table 1. Numbers of nights per month used in the analysis, of special (self-consistent) cases, fraction of cases normalized by number of nights and cases with very long vertical wavelength.

month	# nights	# special	%	#long λ_z
1	155	0	0	0
2	180	6	3.3	0
3	221	10	4.5	0
4	283	25	8.8	0
5	265	23	8.7	4
6	263	22	8.4	5
7	240	22	9.2	2
8	263	23	8.7	1
9	236	11	4.7	1
10	309	14	4.5	0
11	264	3	1.1	1
12	200	0	0	0
total	**2879**	**159**	**5.5**	**14**

For each airglow emission, we calculate the Krassovsky ratio, which is a complex dimensionless number defined as

$$\eta = \frac{A_I / \overline{I}}{A_T / \overline{T}} e^{i\phi},$$

where A_I and $\overline{I}$ are the nocturnal amplitude and mean intensity, A_T and $\overline{T}$ the corresponding values for temperature, and the phase $\phi = \phi_I - \phi_T$ is the difference of the intensity and temperature phases (we define ϕ in the range from -180° to +180°). We evaluate the phase ϕ at the center of the data interval, and so avoid systematic errors due to the small differences of the intensity and temperature frequencies. Note that the original definition of this ratio (Krassovsky, 1972) was the modulus of η used to shed light on the excitation mechanism for OH airglow.

According to the Hines and Tarasick theory (1987) for zenith airglow observations, the vertical wavelength λ_z depends mostly on the imaginary part of η (see RS96):

$$\lambda_z \approx \frac{2\pi\gamma H}{(\gamma-1)|\eta|\sin\phi},$$

where $\gamma = 1.4$ is the ratio of the specific heats and H the scale height. We attach a sign to λ_z, so that a negative λ_z means downward propagation of wave phase (or upward

energy propagation), and of course the opposite for positive λ_z. This approach for determining the vertical wavelength has been used by other investigators (e.g., Guharay et al., 2008; Ghodpage et al., 2016; López-González, 2017).

Note that λ_z has the same sign as ϕ (in our notation). This means that when the temperature phase is advanced with respect to intensity (so that ϕ is negative), the vertical phase propagation is downward. The physical meaning becomes more intuitive when we take the difference between the effective altitudes of the intensity and temperature oscillations into account. According to Swenson and Gardner (1998), *"Fluctuations in the emission rate are largest near the bottomside of the OH* layer..."*, while *"Fluctuations in rotational temperature are largest near the peak of the OH layer where the volume emission rate is largest"*. In other words, the observed variations in the OH band intensity come from a lower altitude than the rotational temperature variations. This altitude separation between intensity and temperature fluctuations is responsible for the phase shift ϕ. Although not discussed by Swenson and Gardner, an analogous (but probably different) separation is expected for the O_2 emission. Since the OH and O_2 layers are centered near 87 and 95 km, respectively, the four measured fluctuations correspond to the following order of effective altitude (from higher to lower): O_2 temperature (TO2), O_2 intensity (IO2), OH temperature (TOH), and OH intensity (IOH). For our mini-review about the Hines and Tarasick theory, see http://www.iafe.uba.ar/aeronomia/HT.HTM.

3. Results

Before entering into a statistical description of our results, we present two examples for individual nights. One is for the shortest nocturnal dataset among the self-consistent cases, with a span of 7.2 hours, unusually short for the time of the year (30 April 1998, in our date notation that refers to the begining of the night). The periods of the fits for the different parameters range from 10.0 to 11.8 h (see Fig. 1). The other example, for the longest dataset, observed on 5 July 2002, has a data span of 11.9 hours, and fitted periods from 10.4 and 12.2 h. Even from visual inspection of the figure, it is clear that other parameters like phase show little scatter.
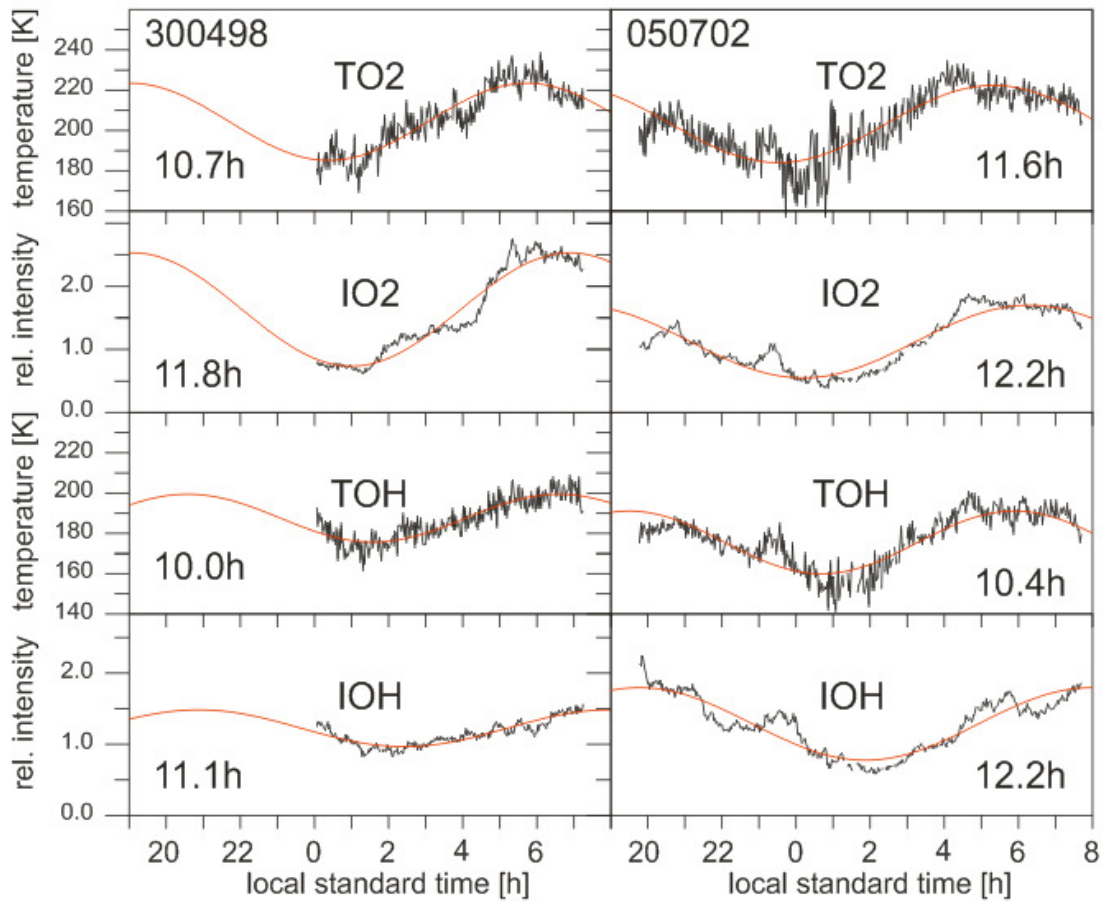
Fig. 1. Examples of data and least-squares fits for the 4 parameters of the self-consistent cases April 4, 1998 (left) and July 5, 2002 (right). Fitted periods are also shown in each panel.

3.1 Periods

All the 159 self-consistent cases turn out to have periods in the tidal period range, between about 9 and 15.5 hours (Fig. 2, with one outlier at 16.5 h). This is a natural result that was not enforced by the analysis. The mean period (based on the average frequency) is 11.8(±0.1)h. Most cases (129) are in the "semidiurnal period range" of 10 to 14 hours (the term used in RS96).
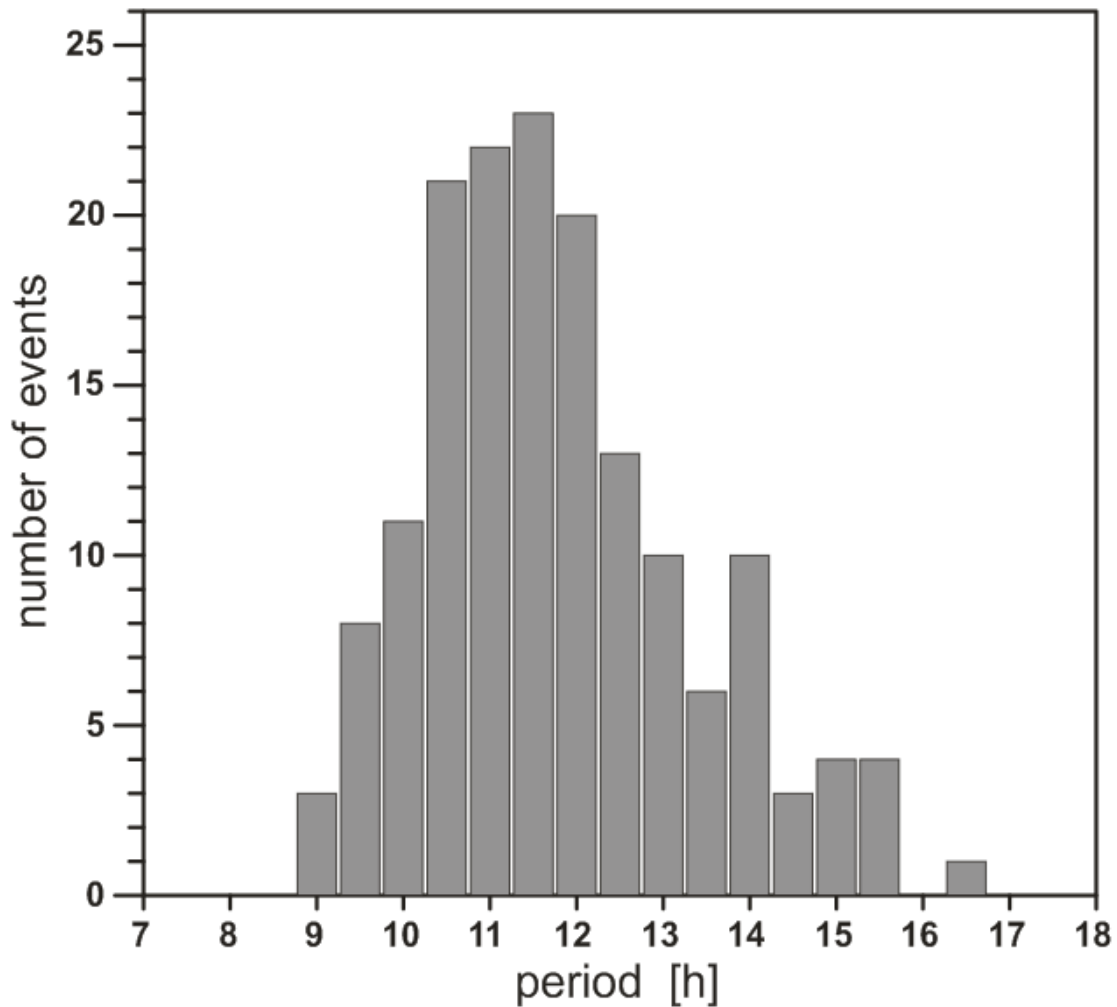
Fig. 2. Histogram of the number of cases versus period (30-min bin size).

3.2 Phases

The observed periods are really manifestations of the semidiurnal tide and not of long-period gravity waves (of the kind described by Meyer and Forbes, 1997). This becomes plausible because of the small range of phases involved. The distributions of the phases are clearly concentrated around fixed values, instead of covering a very wide range (as would be expected for gravity waves). Most phases, expressed as the local time of maximum, occur within one hour of the median value (e.g., 107 cases for TO2, 94 for TOH; only the IOH distribution is slightly wider; see Fig. 3). The figure also shows the phase progression from high to low altitude, consistent with downward phase propagation. This can also be seen in the medians that are 04:24 for TO2, 05:21 for IO2, 05:42 for TOH, and 07:24 for IOH (in local standard time, LST).
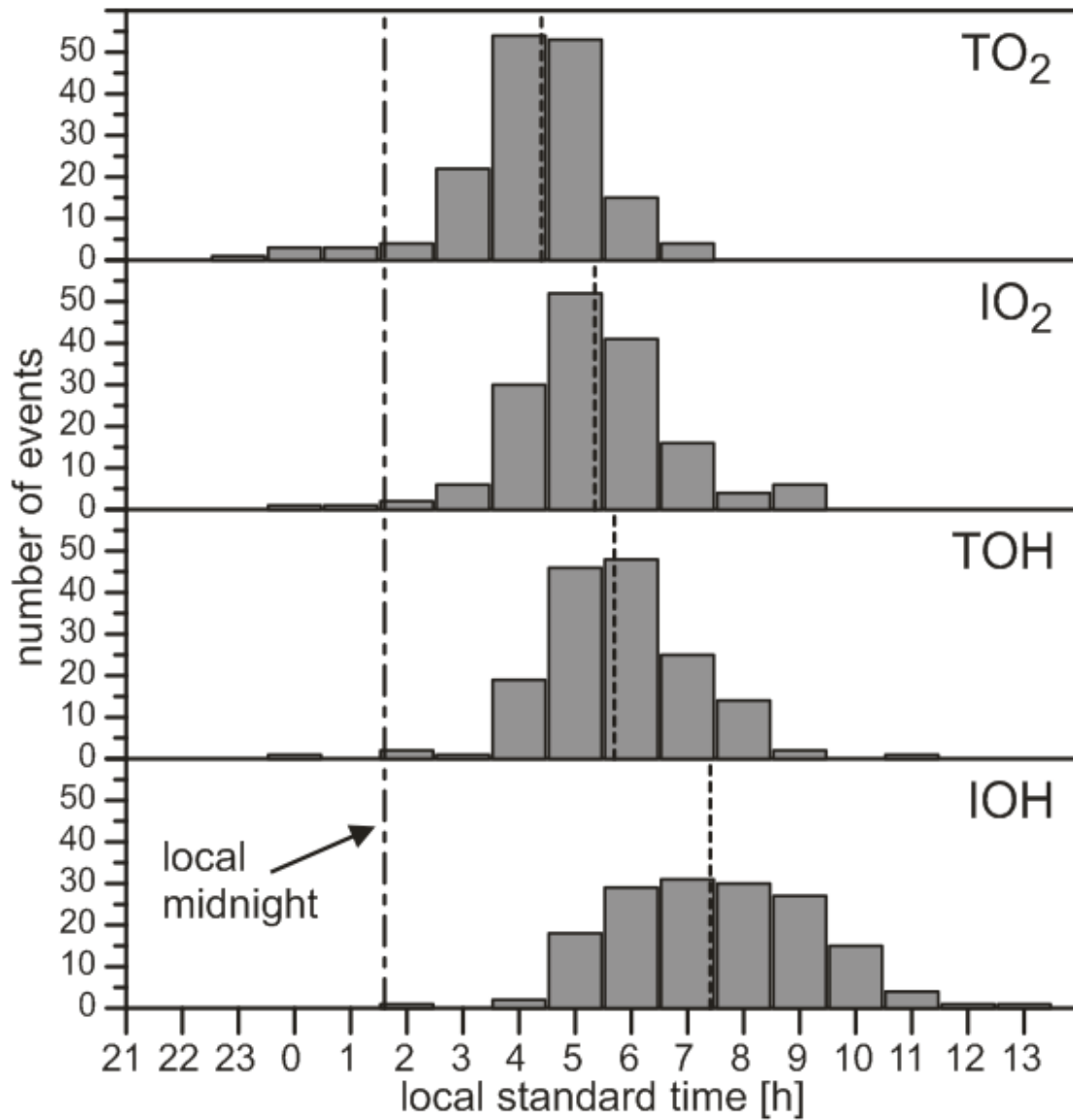
8

Fig. 3. Distribution of phases for the four parameters, treated as if they were independent, and median values (vertical dashed lines). Local midnight at 1:37 LST is also marked.

A better way to see this downward phase propagation, is to follow the phase changes for each individual wave on its way through the four effective height levels. This means, we look at the phase changes between "neighboring" heights (i.e., phase difference between IO2 and TO2, TOH and IO2, or IOH and TOH). These phase differences are mostly positive, that is, the waves at the lower height level are delayed with respect to the wave at the higher level (see Fig. 4). The differences between the medians are 28.4° for $\phi_I(O_2)$ - $\phi_T(O_2)$, 23.1° for $\phi_T(OH)$ - $\phi_I(O_2)$, and 44.6° for $\phi_I(OH)$ - $\phi_T(OH)$. Note that the smallest differences occur between TOH and IO2, which suggests that the effective heights for these two parameters are close together. This would be consistent with the strong similarity between the nocturnal variations of O_2 intensities and OH temperatures, observed in the past (e.g., Scheer, 1995; Scheer and Reisin, 1998; López-González et al., 2017), especially striking for complex waveforms (Smith et al., 2010).
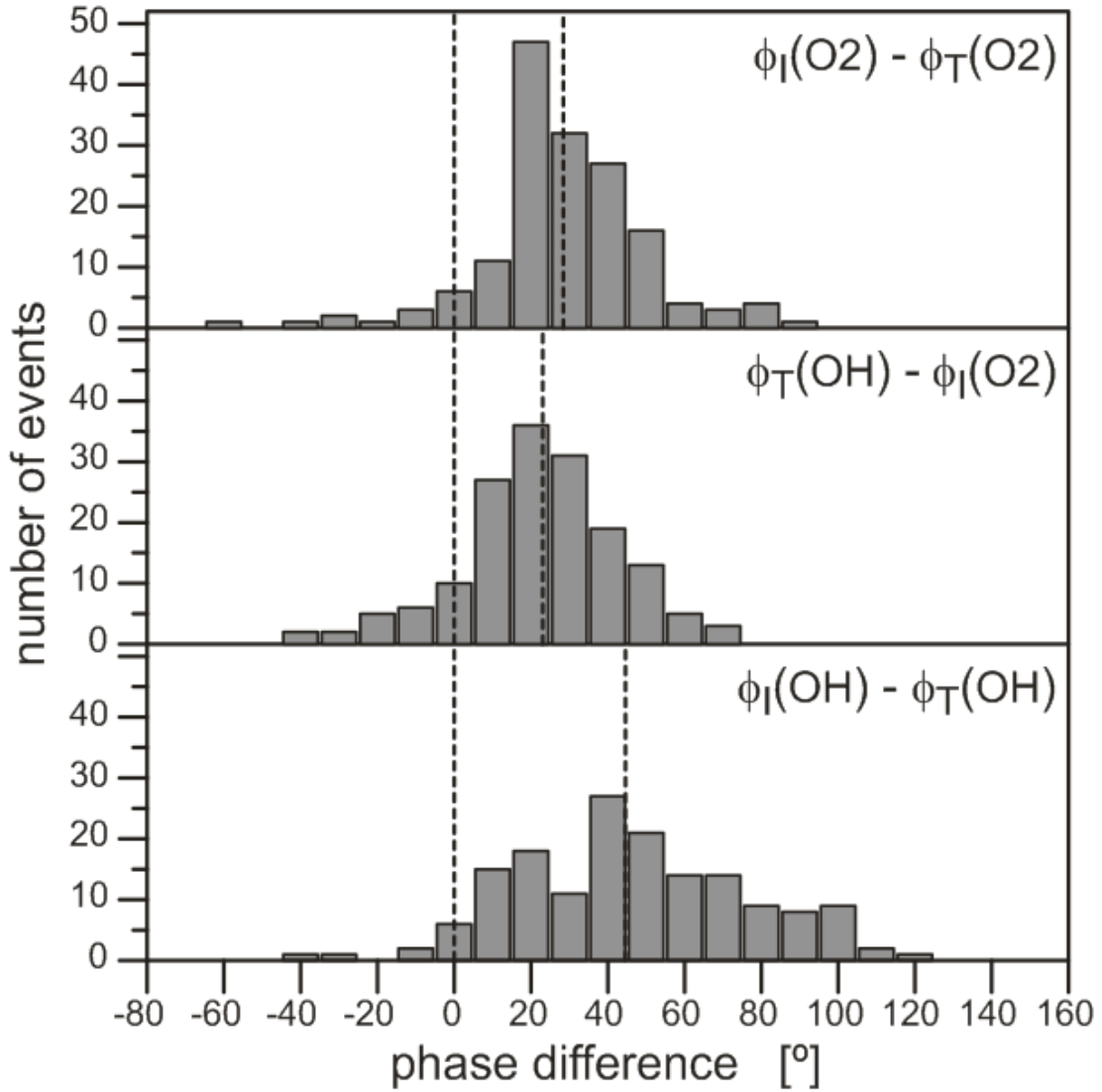
9

Fig. 4. Distribution of phase changes for individual waves between neighboring effective heights, and median values (short dashed lines). Zero phase change is also marked.

3.3 Amplitudes

The mean temperature amplitudes between March and October practically do not vary from month to month, being consistent with the total average within individual error bars (Fig. 5). This total average for TO2 (15.6($\pm$0.7)K) is greater than for TOH (11.4($\pm$0.5)K). Note that our earlier two-layer results (based on 13 self-consistent cases) of 14.9($\pm$1.0)K for O_2 and 12.2($\pm$1.0)K for OH (RS96) are surprisingly similar to the present values, in spite of their partly different geographic origins (see next section).
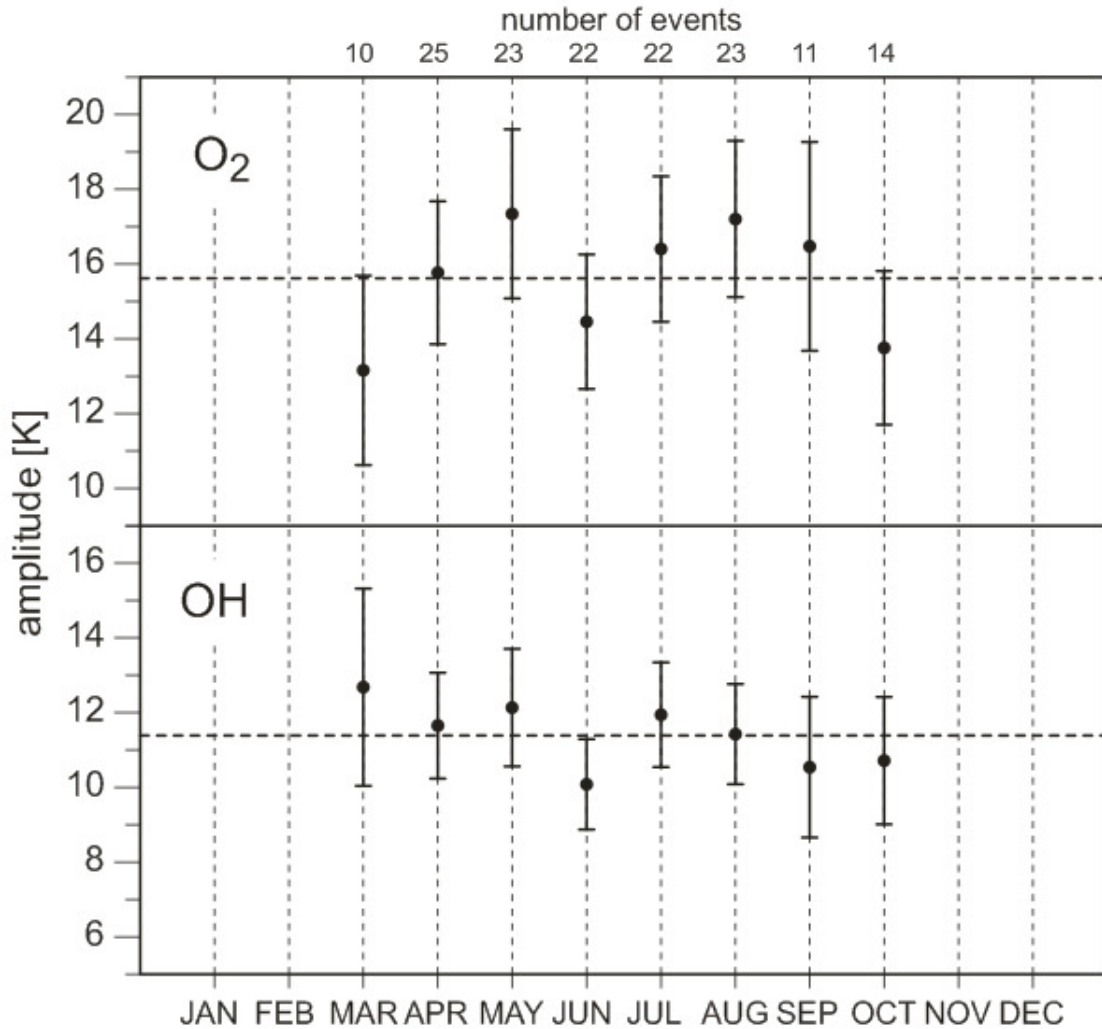
Fig. 5. Monthly averages of temperature amplitudes for O_2 (upper panel) and OH (lower panel), and total means (horizontal dashed lines). The number of events per month is shown on top. Vertical dashed lines to guide the eye.

The present total averages are larger than the climatological monthly mean tides from Reisin and Scheer (2017), which range from 6.1 K to 12.1 K for O_2 and from 4.3 K to 7.5 K for OH. The explanation is simply that while the present results are based on cases with clear tidal signatures simultaneously present in both emissions, the previous results are climatological means that include nights with low tidal amplitude (even nights without tide).

3.4 Krassovsky's ratio

As mentioned, the Hines and Tarasick theory implies that the imaginary part of η is negative for downward phase propagation. Given that the effect of chemistry on the real part of η is small (Reisin, 1994), the η values should be concentrated in the fourth quadrant of the complex plane as we have seen in the past (RS96). This is what also happens with our present results. For O_2, almost all η values are found in the fourth

quadrant (see Fig. 6). There are a few values near the real axis, which may correspond to large vertical wavelengths, standing waves or evanescence. The error bars (here, and in Fig. 7 and Fig. 9) are calculated using the jackknife method (Efron and Gong, 1983). The scatter of the points is greater for OH than for O_2, even with some points in the third quadrant (Fig. 7). This could be due to a chemical contribution to the real part of η (Tarasick and Shepherd, 1992).
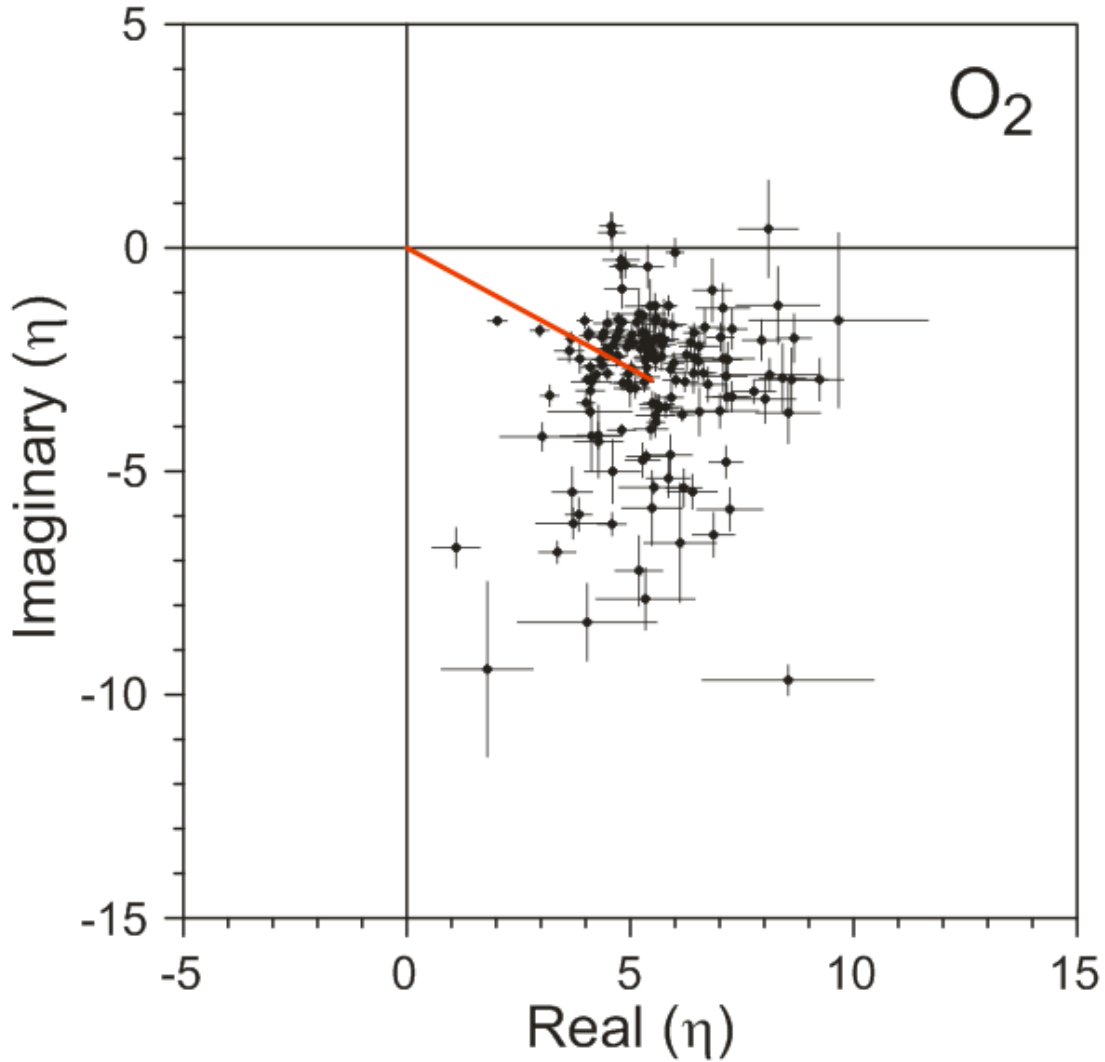

Fig. 6. Distribution of Krassovsky's η for O_2 in the complex plane, and their vectorial mean.

The mean η vectors are $|\eta| = 6.2(\pm0.4)$, $\phi = -28.3(\pm3.1)°$ for O_2 and $|\eta| = 5.3(\pm0.4)$, $\phi = -48.1(\pm3.7)°$ for OH. We can compare these values with our earlier findings (RS96), namely for the semidiurnal period range (10 to 14h) and also the two-layer results (see Table 2). In spite of the different procedures and conditions under which the results were obtained, the values are similar, except for the more negative OH phases, in the past. Note that about one half of the cases in RS96 were from the NH site El Arenosillo in Spain. The present results are considerably more representative of the climatology in El Leoncito, not only because they are based on a greater number of data but also
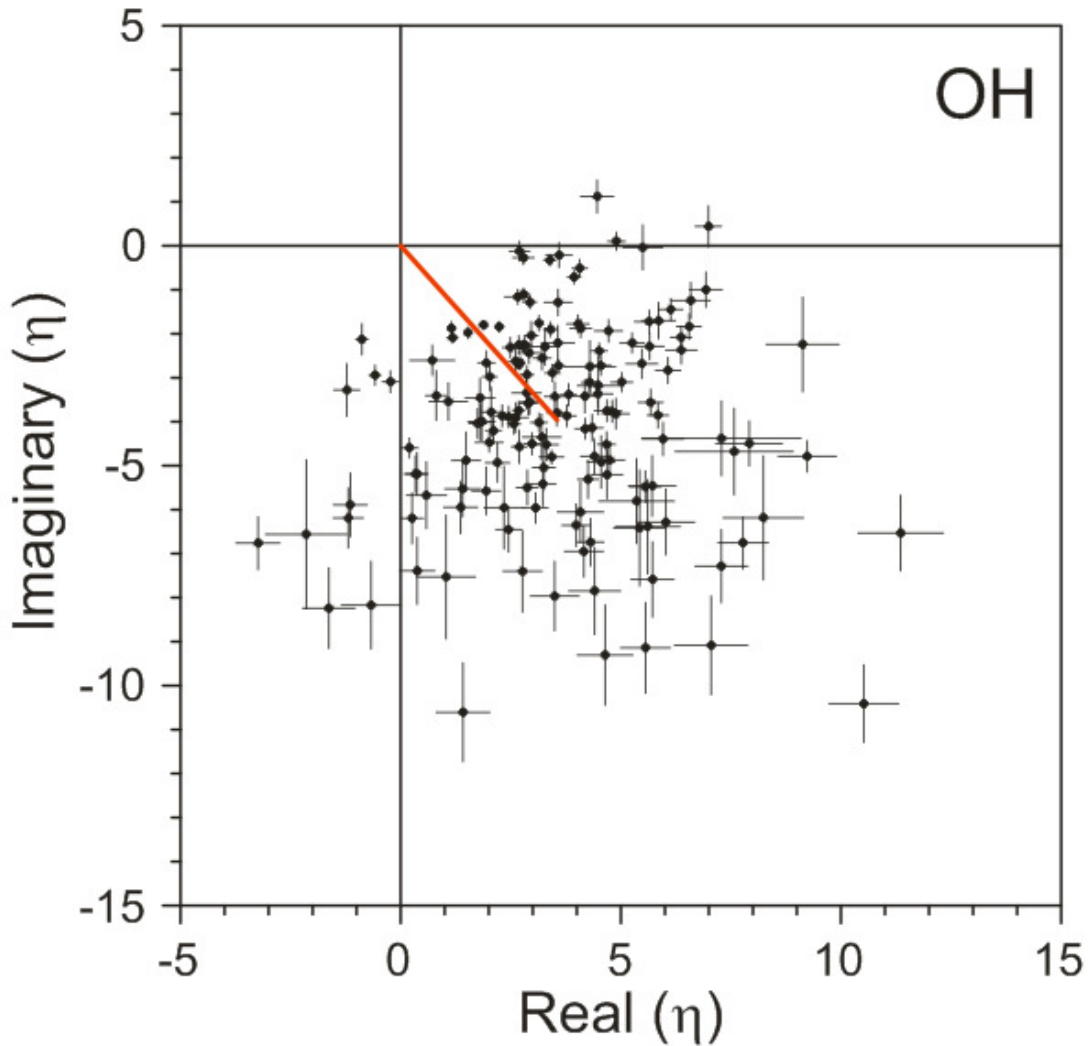
because of better statistical homogeneity.

Fig. 7. As Fig. 6 but for OH.

Table 2. Comparison of the present mean η values (in modulus and phase) with the previous RS96 results for 10-14h period range and for two-layer emission. N is the number of nights involved.

	O$_2$			OH		
	N	$|\eta|$	ϕ	N	$|\eta|$	ϕ
present	159	6.2(±0.4)	-28.3(±3.1)°	159	5.3(±0.4)	-48.1(±3.7)°
RS96 10-14h	19	6.7(±0.3)	-31.5(±3.2)°	15	5.0(±0.6)	-70.3(±6.5)°
RS96 two-lay	13	7.2(±0.5)	-36°	13	5.5(±0.6)	-66°

3.5 Vertical wavelengths

The λ_z distribution for O$_2$ is rather wide with many cases from -70 km to -40 km. The vertical wavelengths for OH tend to be shorter than for O$_2$ (Fig. 8). The distribution of λ_z for OH is narrower, with most cases (101) between -40 km and -10 km. The absence of tides with clear upward phase propagation is evident in Fig. 8, where there are no
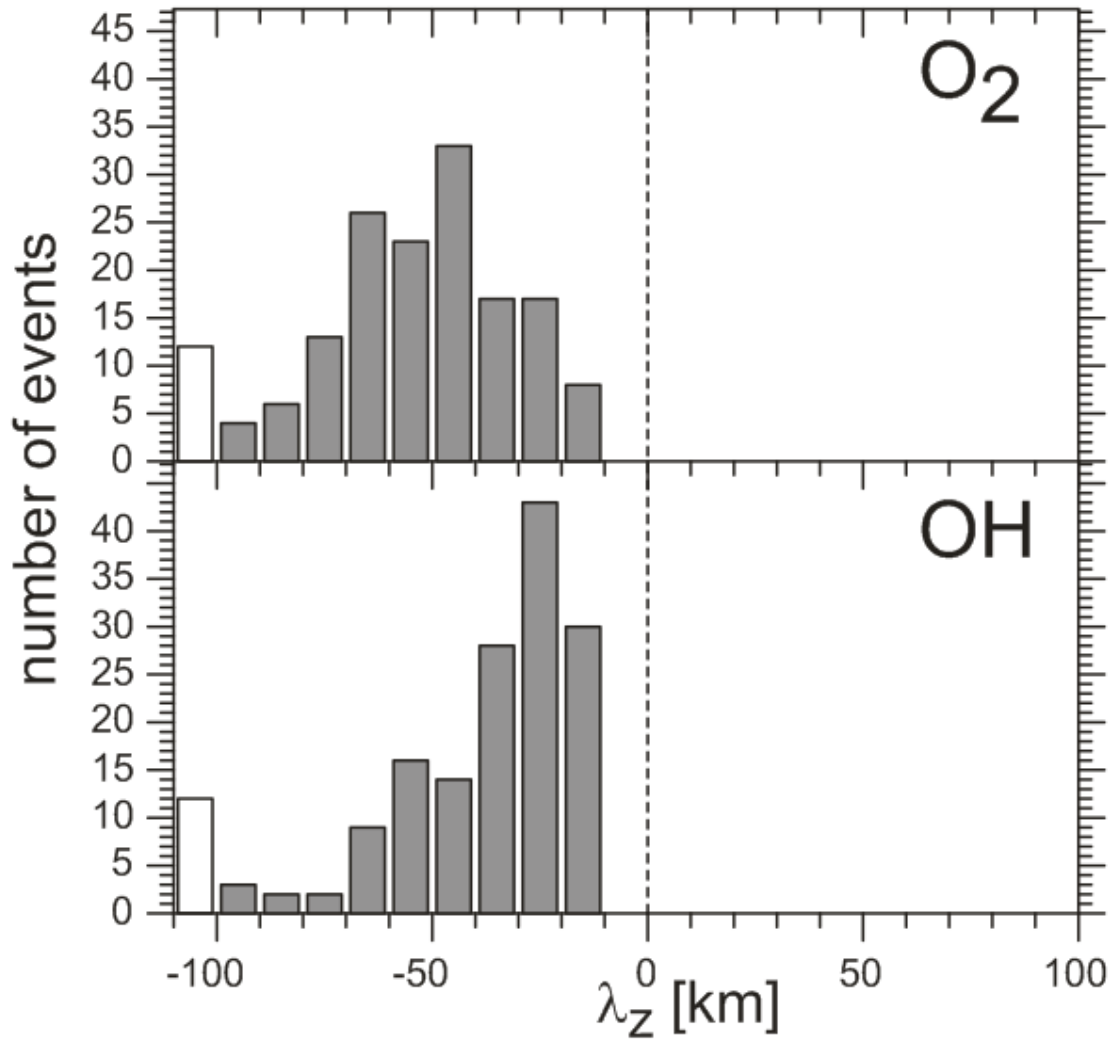
cases with λ_z between 0 and +100km.

.

Fig. 8. Distribution of vertical wavelength for O_2 (top) and OH (botton) with 10km bin size. Very long wavelengths are represented by the empty bars (see text for details).

The mean vertical wavelength (inferred from the mean wavenumber) for O_2 is -41.8 (±1.8)km (where some cases with extreme vertical wavelength, as discussed below, have been excluded). This is only marginally higher than our old result of -36.4(±3.1)km (Table 2 of RS96). The present value for OH is -27.6(±1.1)km, equal to -27.7(±2.8)km from RS96.

An earlier study based on 12-hour horizontal wind oscillations observed optically in New Zealand at 44ºS (Hernandez et al., 1995) in OH and the atomic oxygen green line emission, supported by emission altitudes measured from the UARS satellite, had already obtained vertical wavelengths between 20 and 40 km during most of the year. Our present results are consistent with these short wavelengths, obtained with a completely different technique, but at a similar latitude.

14

The mean vertical wavelengths obtained by López-González et al. (2017), of 33(±18)km for O_2 and 35(±20)km for OH, also based on the Hines and Tarasick theory, are consistent with our results within their large error bars.

We find no cases with vertical wavelengths shorter than 10 km (Fig. 8). This can be explained by phase cancellation for vertical wavelengths in the order of the airglow layer width. According to Swenson and Gardner (1998), the cancellation factor for TOH perturbations and $|\lambda_z| < 10$ km is less than 0.02 (see their Fig. 11), which means a reduction of the observed wave amplitude by more than 98% of the true value.

With respect to the extreme vertical wavelengths mentioned, we see 12 cases with vertical wavelength longer than 100 km, for each of the two emissions (the empty bars at the left-hand side of Fig. 8 combine $|\lambda_z| > 100$ km for both signs of λ_z). Ten of these cases were observed simultaneously in both emissions. In the remaining nights a wavelength longer than 100 km was identified in one emission but not in the other. However, these are still accompanied by large vertical wavelengths ($|\lambda_z| > 68$ km) in the other emission and they are indistinguishable within error bars. Therefore, all the 14 nights involved are part of the same long-wavelength class.

Rather than only a statistical comparison between the vertical wavelengths for both emissions considered separately and independently as discussed above, we now use the fact that the tide is here always observed at both altitudes, which is not expressed in the histograms of Fig. 8. This means that we can directly compare, for each of the nights, the vertical wavelength of the OH tide with the respective one for O_2. We do this by plotting vertical wavenumbers (k_z) of OH versus O_2 (Fig. 9; we exclude the 14 cases of extreme wavelength to avoid some minor clutter).
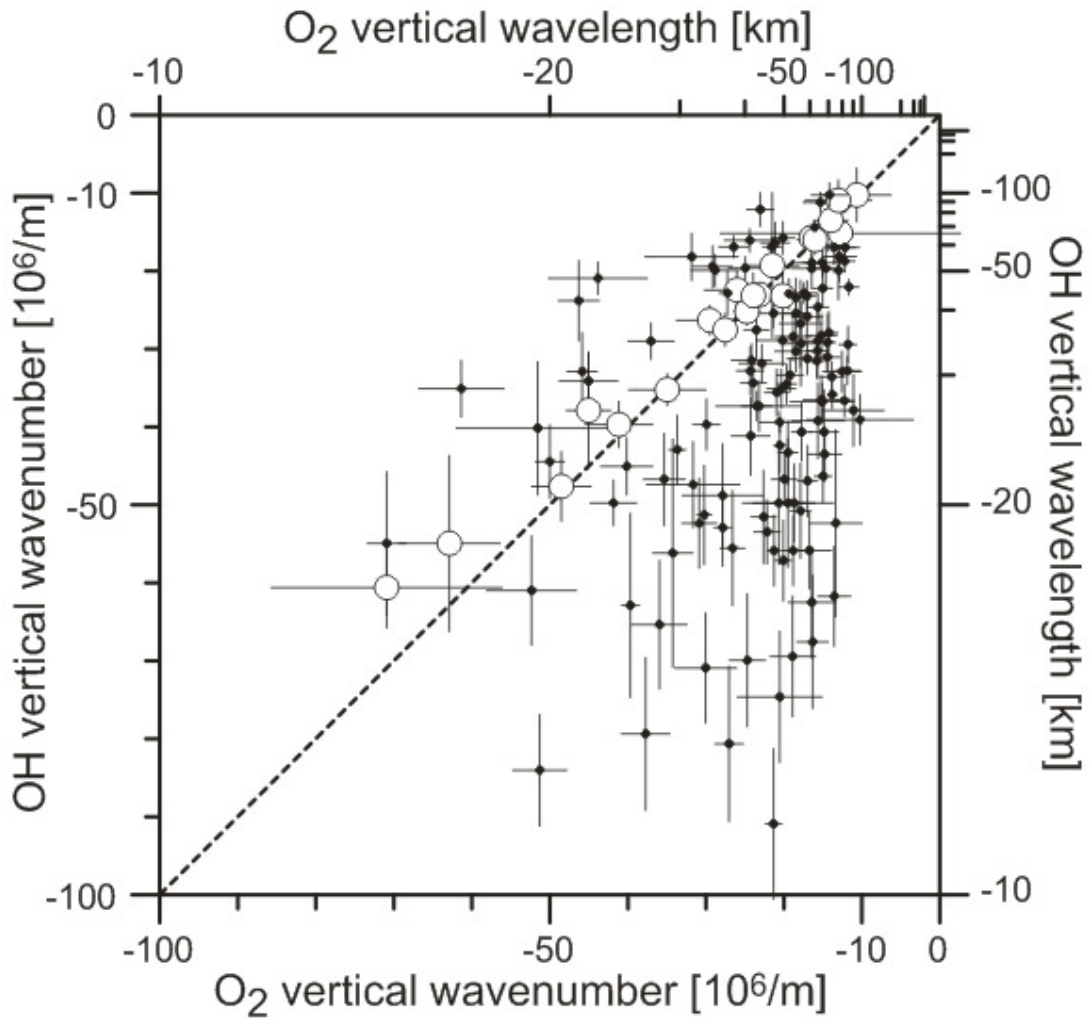
Fig. 9. Vertical wavenumbers for OH versus v.w. for O_2, with jackknife error bars. Equal vertical wavenumber cases are highlighted as open circles. Note also the nonlinear wavelength scales.

The tendency of vertical wavelengths to be greater for O_2 than for OH, already mentioned, is more clearly visible in Fig. 9 where most points are to the right-hand side of the diagonal $k_z(OH) = k_z(O_2)$. There are 101 points where λ_z is longer for O_2 than for OH, and only 23 points for the opposite situation. On the other hand, there are 21 cases with equal vertical wavelength for both emissions, within error bars (big circles of Fig. 9). The reason for the difference is not obvious, but it could be related to different vertical wavelengths for different tidal modes. If the tidal mode composition varies with altitude, the mean vertical wavelength would also change.

We can also analyze the seasonal variation of vertical wavelength. Again, we exclude the cases with extreme wavelengths, and do not take the months with scarce data (November to February) into account. For both emissions, mean wavelengths are longest from May to August, and smallest near the equinoxes. The monthly averages for the OH emission range between 30 to 36 km from May to August (see Fig. 10). They range between 20 and 24 km for March and April, and also for September and October.

For O_2, the monthly averages are between 46 and 53 km from May to September, and between 27 and 39 km for March, April and October. That is, mean vertical wavelengths for O_2 are greater than for OH, not only in general, as mentioned above, but also in each of these individual months. Such a seasonal variation of vertical wavelength of the semidiurnal tide is difficult to relate to the existing literature, as far as we know.
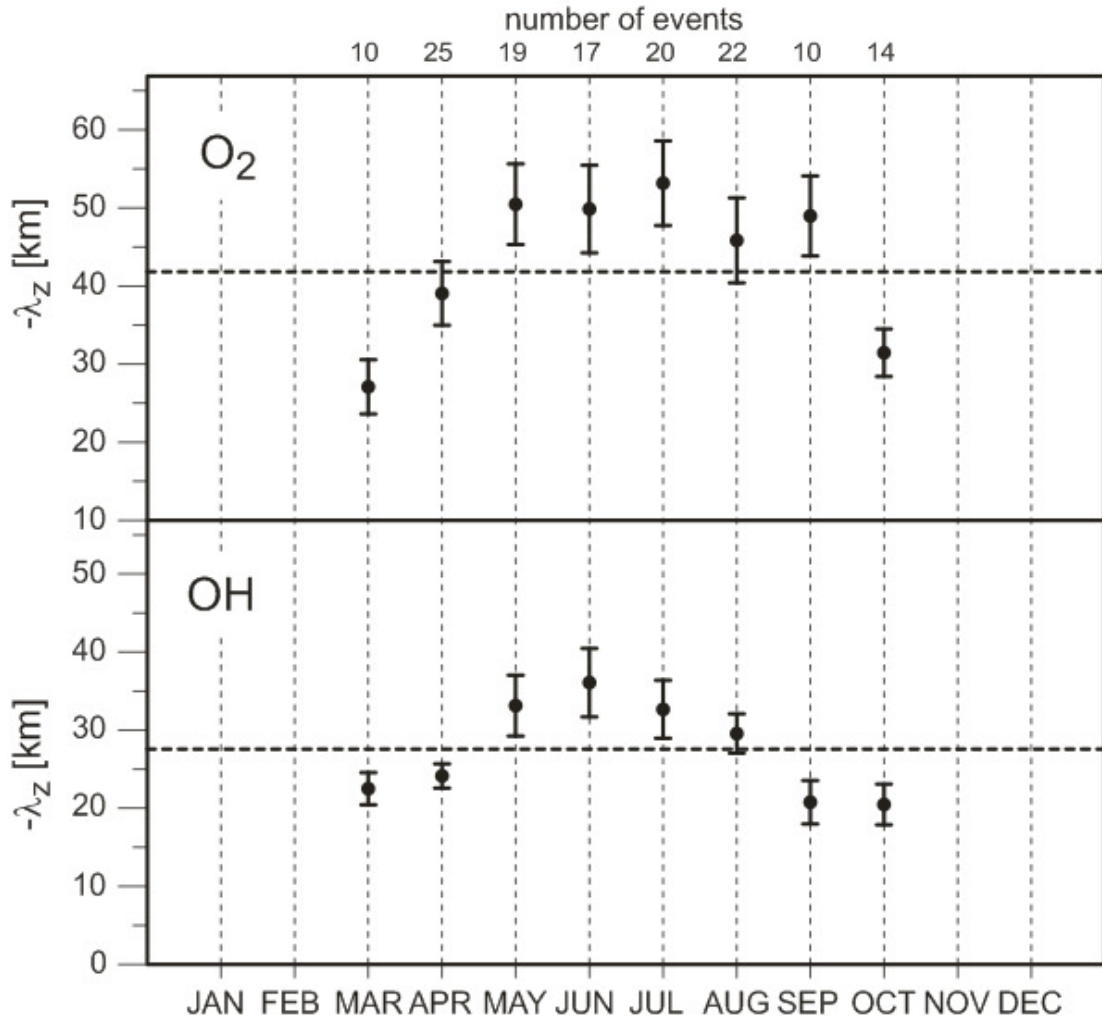

Fig. 10. As Fig. 5, but for vertical wavelength (note the suppressed negative signs).

3.6 Layer separation

The separation between the O_2 and OH layers (Δz) can be estimated for each night from the mean vertical wavelength (calculated as the inverse of the average of the O_2 and OH angular wavenumbers $<k>$) and the phase difference $\Delta\phi$ between the intensity (or temperature) oscillations of both emissions ($\Delta z = \Delta\phi / <k>$). Since the vertical wavelengths are more than twice as long as the expected layer separation, this estimation works well for all the nights. We find a mean Δz value of 7.06($\pm$0.21)km for intensity, and 4.84($\pm$0.19)km for temperature. These values are similar to the respective

17

7.26(±0.9)km and 4.58(±0.5)km reported in RS96. The reason why the values of Δz derived from intensity and temperature are different, while related to the different effective altitudes for the four parameters, can not be understood with the information presently available. So, this remains an open question for future research.

3.7 Growth factors

Our data can also be used to produce 159 independent values for the growth factor, defined as the ratio between temperature amplitudes of O_2 and OH. The resulting mean growth factor is 1.42(±0.04), only slightly higher than the 1.27(±0.07) value obtained in RS96. It is consistent with the value of 1.1(±0.5) reported by López-González et al. (2017), within its error bar. In the absence of attenuation, this factor can be calculated as $e^{\Delta z/2H}$, where Δz is the vertical separation between the two layers. With $H \approx 6$ km and the mean Δz for temperature, 4.84 km, we obtain 1.50 as the attenuation-free growth factor. While the present mean growth factor corresponds to a moderate attenuation, the wide scatter of the data ($\sigma = 0.45$) means that there are also many cases of growth factor smaller than one, corresponding to very strong attenuation. There are also cases with growth factors greater than 1.50, which may be due to higher effective layer separations. For example, growth factors of about 1.8 can be explained by Δz in the order of 7 km, without attentuation.

In terms of the monthly values of the growth factor, most points are consistent with the total mean amplitude ratio of 1.42, except for a low value in March (1.18±0.15) and a high value in September (1.67±0.15; see Fig. 11).
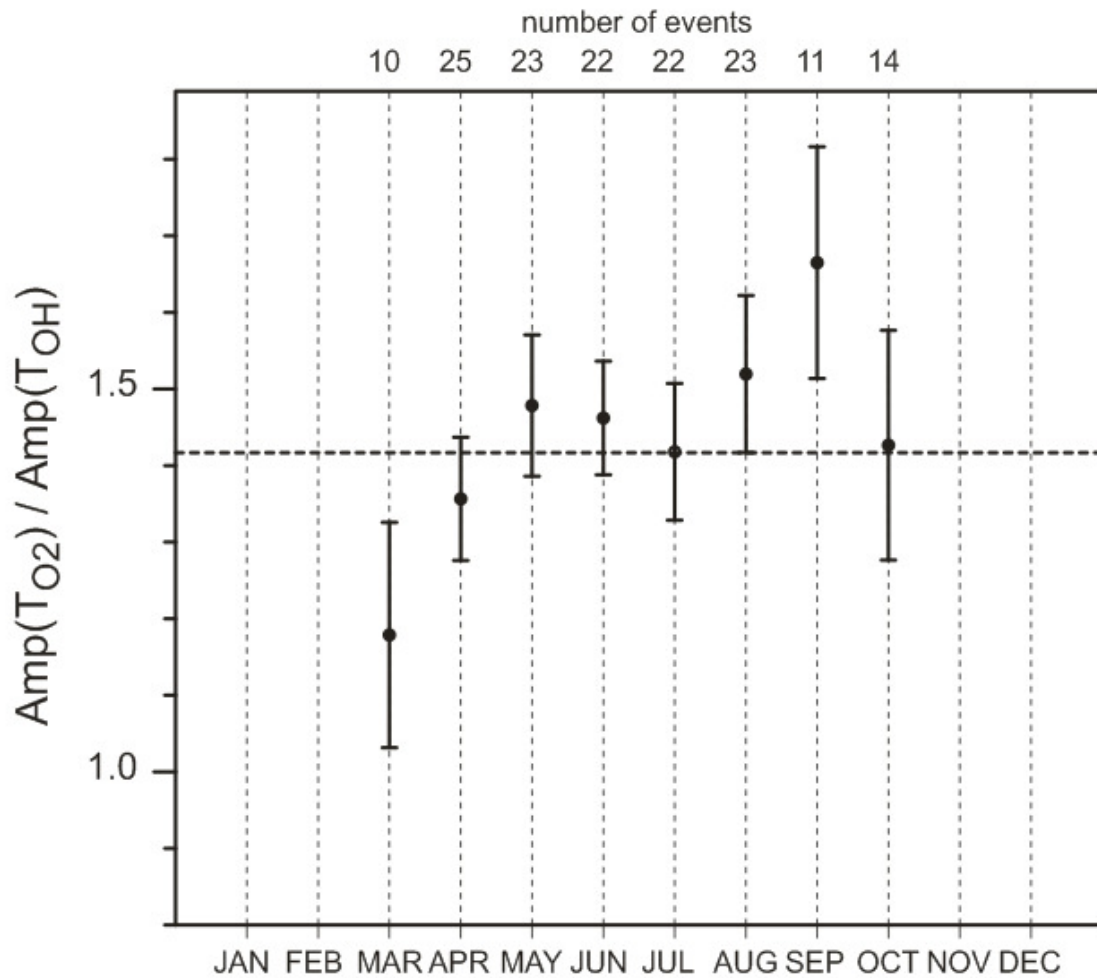
Fig. 11. Monthly mean ratios between O_2 and OH temperature amplitudes, and total mean (horizontal dashed lines). Other details as Fig. 5.

4. Conclusions

From our dataset of O_2 and OH band intensities and rotational temperatures spanning the years from 1998 to 2014, we have extracted data for 159 single nights that document the semidiurnal tide consistently in the four parameters. This number of cases is an improvement of more than twenty times with respect to our earlier results from El Leoncito (RS96). From April to August, about 9% of the nocturnal data scrutinized belong to this class of self-consistent cases.

The identification of the semidiurnal tide in the nocturnal variations is based on the narrow distribution of phases and the downward phase propagation observed in almost all cases.

The mean temperature amplitudes of the 159 cases are considerable, amounting to 15.6($\pm$0.7)K for O_2 and 11.4($\pm$0.5)K for OH. The monthly averages from March to October, which we are only now in a condition to define, are all close to these mean levels.

19

The individual values for Krassovsky's ratio η are concentrated in the fourth quadrant of the complex plane, as expected from the Hines and Tarasick theory for waves with downward phase propagation, and confirming earlier results. We obtain the following vectorial means for the modulus and phase of Krassovsky's ratio: $|\eta| = 6.2(\pm0.4)$, $\phi = -28.3(\pm3.1)°$ for O_2 , and $|\eta| = 5.3(\pm0.4)$, $\phi = -48.1(\pm3.7)°$ for OH.

In comparison with model results for the semidiurnal tide, our mean vertical wavelengths are rather short, namely $-41.8(\pm1.8)$km for O_2 and $-27.6(\pm1.1)$km for OH, but they are similar to some observations by other researchers. There is a tendency for vertical wavelengths to be longer for O_2 than for OH, which is possibly related to changes in the tidal mode composition at different altitudes.

There are only 14 cases (not included in the means) with very long vertical wavelengths that may be due to standing or evanescent waves.

As another original result, we find the longest monthly mean wavelengths from May to August (close to 50 km for O_2 and 33 km for OH), and smallest near the equinoxes (about 34 km for O_2 and 22 km for OH).

The vertical wavelengths are used to estimate the mean separation between both layers and we arrive at two different results when intensity or when temperature phases are compared. The mean separation between the O_2 and OH layers is $7.06(\pm0.21)$km for intensity, and $4.84(\pm0.19)$km for temperature. This disagreement, already discovered in RS96, may be related to the different effective altitudes of the intensity and temperature oscillations for both emissions.

The ratio between the temperature amplitudes for O_2 and OH represents the growth factor of the tide as it propagates upwards. We find a mean growth factor of $1.42(\pm0.04)$, consistent with moderate attenuation.

We hope to have shown the advantages of limiting the analysis to the self-consistent subset of results with similar periods in the two emission layers to determine the characteristics of the semidiurnal tide at a fixed site.

References

Azeem, I., Walterscheid, R. L., Crowley, G., Bishop, R. L., Christensen, A. B., 2016. Observations of the migrating semidiurnal and quaddiurnal tides from the RAIDS/NIRS instrument. J. Geophys. Res., 11, 4626-4637, doi:10.1002/2015JA022240

Conte, J.F., Chau, J.L., Laskar, F.I., Stober, G., Schmidt, H., Brown, P., 2018. Semidiurnal solar tide differences between fall and spring transition times in the Northern Hemisphere. Ann. Geophys., 36, 999-1008, doi:10.5194/angeo-2018-29.

Efron, B., Gong, G., 1983. A leisurely look at the bootstrap, the jackknife, and cross-validation. The American Statistician, 37(1), 36-48.

Fisher, G.M., Niciejewski, R.J., Killeen, T.L., Gault, W.A., Shepherd, G.G., Brown, S., Wu, Q., 2002. Twelve-hour tides in the winter northern polar mesosphere and lower thermosphere. J. Geophys. Res., 107(A8), 1211, doi:10.1029/2001JA000294.

Forbes, J.M., Russell, J., Miyahara, S., Zhang, X., Palo, S., Mlynczak, M., Mertens, C.J., Hagan, M.E., 2006. Troposphere-thermosphere tidal coupling as measured by the SABER instrument on TIMED during July-September 2002. J. Geophys. Res., 111(A10), A10S06, doi:10.1029/2005JA011492.

Ghodpage, R.N., Hickey, M.P., Taori, A.K., Siingh, D., Patil, P.T., 2016. Response of OH airglow emissions to mesospheric gravity waves and comparisons with full-wave model simulation at a low-latitude Indian station. Atmos. Chem. Phys., 16, 5611-5621.

Guharay, A., Taori, A., Taylor, M., 2008. Summer-time nocturnal wave characteristics in mesospheric OH and O2 airglow emissions. Earth Planets Space, 60, 973-979.

Hernandez, G., Wiens, R., Lowe, R. P., Shepherd, G. G., Fraser, G. J., Smith, R. W., LeBlanc, L. M., Clark, M., 1995. Optical determination of the vertical wavelength of propagating 12-hour period upper atmosphere oscillations. Geophys. Res. Lett., 22, 2389-2392.

Hines, C.O., Tarasick, D.W., 1987. On the detection and utilization of gravity waves in airglow studies. Planet. Space Sci., 35(7), 851-866.

Krassovsky, V.I., 1972. Infrasonic variations of OH emission in the upper atmosphere. Annales de Géophysique, 28(4), 739–746.

Lomb, N.R., 1976. Least-squares frequency analysis of unequally spaced data. Astrophys. Space Sci., 39, 447-462.

López-González, M. J., Rodriguez, E., Shepherd, G. G., Sargoytchev, S., Shepherd, M. G., Aushev, V. M., Brown, S., Garcia-Comas, M., Wiens, R. H., 2005. Tidal variations of O_2 Atmospheric and OH(6-2) airglow and temperature at mid-latitudes from SATI observations. Ann. Geophys., 23, 3579-3590.

López-González, M.J., Rodríguez, E., Garcia-Comas, M., López-Puertas, M., Olivares, I., Ruiz-Bueno, J.A., Shepherd, M.G., Shepherd, G.G., Sargoytchev, S., 2017. Semidiurnal tidal activity of the middle atmosphere at mid-latitudes derived from O_2 Atmospheric and OH(6-2) airglow SATI observations. J. Atmos. Solar-Terr. Phys., 164, 116-126, doi:10.1016/j.jastp.2017.08.014.

Meyer, C. K., Forbes, J. M., 1997. Natural oscillations of the ionosphere-thermosphere-mesosphere (ITM) system. J. Atmos. Solar-Terr. Phys., 59, 2185-2202.

Mulligan, F.J., Nallen, J.J., 1998. A search for evidence of tidal activity in OH(3,1) airglow emissions recorded at Maynooth (53.23° N, 6.35° W). Adv. Space Res., 21(6), 831-834.

Pancheva, D., Mukhtarov, P., Andonov, B., 2009. Global structure, seasonal and interannual variability of the migrating semidiurnal tide seen in the SABER/TIMED temperatures (2002-2007). Ann. Geophys., 27, 687-703.

Reisin, 1994. Estudio de las ondas atmosfericas en la region de la mesopausa a partir de las temperaturas rotacionales de OH(6-2) y de O_2b(0-1). Doctoral Thesis, Universidad de Buenos Aires, October 1994.

Reisin, E. R., Scheer, J., 1996. Characteristics of atmospheric waves in the tidal period range derived from zenith observations of O_2(0-1) Atmospheric and OH(6-2) airglow at lower midlatitudes. J. Geophys. Res., 101, 21223-21232.

Reisin, E. R., Scheer, J., 2001. Vertical propagation of gravity waves determined from zenith observations of airglow. Adv. Space Res., 27(10), 1743- 1748.

Reisin, E. R., Scheer, J., 2017. Unexpected East-West effect in mesopause region SABER temperatures. J. Atmos. Solar-Terr. Phys., 157-158, 35-41.

Scheer, J., 1987. Programmable tilting filter spectrometer for studying gravity waves in the upper atmosphere. Appl. Opt., 26, 3077-3082.

Scheer, J., Reisin, E.R., 1990. Rotational temperatures for OH and O_2 airglow bands measured simultaneously from El Leoncito (31°48'S). J. Atmos. Terr. Phys., 52, 47-57.

Scheer, J., Reisin, E. R., Espy, J. P., Bittner, M., Graef, H. H., Offermann, D., Ammosov, P. P., Ignatyev, V. M., 1994. Large-scale structures in hydroxyl rotational temperatures during DYANA. J. Atmos. Terr. Phys., 56, 1701-1715.

Scheer, J., 1995. What can be learned from rotational temperatures derived from ground-based airglow observations about the aeronomy of the Southern Hemisphere. Adv. Space Res., 16, (5)61-(5)69.

Scheer, J., Reisin, E. R., 1998. Extreme intensity variations of O_2b airglow induced by tidal oscillations. Adv. Space Res., 21(6), 827-830.

Scheer, J., Reisin, E.R., 2001. Refinements of a classical technique of airglow spectroscopy. Adv. Space Res., 27(6-7), 1153-1158.

Smith, S. M., Baumgardner, J., Mertens, C. J., Russell, J. M., Mlynczak, M. G., and Mendillo, M. Mesospheric OH temperatures: Simultaneous ground-based and SABER OH measurements over Millstone Hill. Adv. Space Res., 45, 239-246, 2010.

Swenson, G. R., Gardner, C. S., 1998. Analytical models for the responses of the mesospheric OH* and Na layers to atmospheric gravity waves. J. Geophys. Res., 103, 6271-6294.

Takahashi, H., Gobbi, D., Batista, P. P., Melo, S. M. L., Teixeira, N. R., Buriti, R. A., 1998. Dynamical influence on the equatorial airglow observed from the South American sector. Adv. Space Res., 21, 817-825.

Tarasick, D. W., Shepherd, G. G., 1992. Effects of gravity waves on complex airglow chemistries. 2. OH emission. J. Geophys. Res., 97, 3195-3208.